Biochemistry **2007,** *46,* 10433−10443

Articles

High-Affinity Homologous Peptide Nucleic Acid Probes for Targeting a Quadruplex-Forming Sequence from a *MYC* Promoter Element[†]

Subhadeep Roy,[‡] Farial A. Tanious,[§] W. David Wilson,[§] Danith H. Ly,[‡] and Bruce A. Armitage*,[‡]

Department of Chemistry, Carnegie Mellon University, 4400 Fifth Avenue, Pittsburgh, Pennsylvania 15213-3890, and Department of Chemistry, Georgia State University, Atlanta, Georgia 30303

Received May 5, 2007; Revised Manuscript Received July 6, 2007

ABSTRACT: Guanine-rich DNA and RNA sequences are known to fold into secondary structures known as G-quadruplexes. Recent biochemical evidence along with the discovery of an increasing number of sequences in functionally important regions of the genome capable of forming G-quadruplexes strongly indicates important biological roles for these structures. Thus, molecular probes that can selectively target quadruplex-forming sequences (QFSs) are envisioned as tools to delineate biological functions of quadruplexes as well as potential therapeutic agents. Guanine-rich peptide nucleic acids have been previously shown to hybridize to homologous DNA or RNA sequences forming PNA−DNA (or RNA) quadruplexes. For this paper we studied the hybridization of an eight-mer G-rich PNA to a quadruplex-forming sequence derived from the promoter region of the *MYC* proto-oncogene. UV melting analysis, fluorescence assays, and surface plasmon resonance experiments reveal that this PNA binds to the *MYC* QFS in a 2:1 stoichiometry and with an average binding constant $K_a = (2.0 \pm 0.2) \times 10^8$ M^{-1} or $K_d = 5.0$ nM. In addition, experiments carried out with short DNA targets revealed a dependence of the affinity on the sequence of bases in the loop region of the DNA. A structural model for the hybrid quadruplex is proposed, and implications for gene targeting by G-rich PNAs are discussed.

Guanine-rich DNA or RNA molecules with at least four tracts of G_n bases ($n = 2-4$) fold into secondary structures known as quadruplexes (*1*, *2*). These structures are based on the formation of G-tetrads, a square planar arrangement of four guanines, hydrogen bonded in a cyclic fashion. π-Stacking of these tetrads and coordination to a central monovalent metal ion lead to further stabilization of the structure. Whereas the first reports of quadruplex structures were published nearly two decades ago (*3*, *4*), these structures have been recently implicated in a variety of biological contexts including promoter regions of genes (*5*−*8*), telomeric ends of chromosomes (*9*−*11*), and alternative splice sites of mRNA (*12*, *13*). Bioinformatics reports (*14*, *15*) indicate the presence of $>10^5$ sequences in the human genome capable of folding into quadruplexes. Additionally, as Huppert et al. have demonstrated (*16*), such sequences are particularly prevalent in promoter sequences of human genes. The most direct evidence of the biological role of quadruplexes has been reported by Paeschke et al. (*17*), who demonstrated the *in vivo* formation of quadruplexes in telomeres of *Stylochnia lemnae* under the control of telomere-binding proteins.

Due to the growing awareness of the biological importance of quadruplexes, there is an urgent need to develop ligands that are able to bind specifically either to these structures or, more generally, to quadruplex-forming sequences (QFSs).[1] Such compounds are desired both as potential therapeutics and as tools for delineating the biological roles of quadruplexes. Prior strategies for targeting quadruplexes include (1) small molecules with large aromatic surfaces that can bind through π-stacking to the guanine tetrads (*18*−*23*), (2) molecules that bind selectively to the grooves of the quadruplex structure (*23*, *24*), and (3) C-rich complementary oligonucleotides (*25*, *26*). Recent work from our laboratory relies on an alternative strategy using G-rich, homologous peptide nucleic acid (PNA) oligomers that are able to form hybrid PNA−DNA or PNA−RNA quadruplexes (*27*−*29*). In this approach, guanines from both the PNA probe and the DNA or RNA target participate in G-tetrad formation, leading to the assembly of extremely stable hybrid quadruplexes. This methodology was first demonstrated by formation of a four-stranded PNA_2-DNA_2 quadruplex by homologous $G_4T_4G_4$ sequences (*27*). Subsequently, a 7-mer PNA sequence with two G_2 tracts was found to bind in a 2:1 stoichiometry to a quadruplex-forming RNA aptamer containing four G_2 tracts (*28*, *29*).

[†] This research was supported by the National Institutes of Health (RO1 GM58547 to B.A.A. and RO1 GM61587 to W.D.W.).

* Author to whom correspondence should be addressed [telephone (412) 268-4196; fax (412) 268-1061; e-mail army@andrew.cmu.edu].

[‡] Carnegie Mellon Universtiy.

[§] Georgia State University.

[1] Abbreviations: QFS, quadruplex-forming sequence; PNA, peptide nucleic acid; TO, thiazole orange; SPR, surface plasmon resonance.

10.1021/bi700854r CCC: $37.00

In this paper we describe studies using homologous PNA probes to target a QFS derived from the promoter region of the human *MYC* gene known as the nuclease hypersensitivity element III$_1$ (NHE III$_1$) (*30*, *31*). This is a sequence of 27 bases that is found upstream of the P1 promoter and known to control 80% of *MYC* expression. The myc protein is a transcription factor that controls the expression of a large number of genes (*32*, *33*). Genetic abnormalities leading to overexpression of myc are key precursors to cellular proliferation in many types of cancer (*34*−*36*), making it a very attractive target for development of therapeutic strategies. Siddiqui-Jain et al. (*37*) have provided evidence suggesting that the formation of a quadruplex by the NHE III$_1$ *in vivo* causes repression of *MYC* transcription. Therefore, probes that are able to selectively recognize this QFS have potential as therapeutics as well as for investigating the role of the NHE III$_1$.

This paper describes results from UV melting, fluorescence, and surface plasmon resonance biosensor studies that demonstrate the formation of extremely stable PNA−DNA hybrid quadruplexes between an 8-mer G-rich PNA and a QFS derived from the NHE III$_1$. Furthermore, studies with short G-rich DNA targets demonstrated that small changes in the non-G portion of the target sequence can lead to significantly different binding affinities of a homologous PNA probe. On the basis of this sequence selectivity and CD spectroscopic results, we present a possible structure for the PNA$_2$−DNA hybrid quadruplex and discuss implications of this high-affinity binding mode for biological applications in regulating gene expression.

EXPERIMENTAL PROCEDURES

Materials. DNA oligonucleotides were purchased from Integrated DNA Technologies (www.idtdna.com) and used without further purification except for biotinylated and fluorescein-labeled DNA, which was purified by HPLC. t-Boc-protected peptide nucleic acid monomers were purchased from Applied Biosystems and used for standard solid-phase synthesis (*38*, *39*) of the PNA oligomers. (PNA monomers are no longer sold by this company.) For PNA attached to thiazole orange, a carboxylic acid derivative of thiazole orange was coupled to the PNA prior to cleavage using the same procedure as for all of the other monomers. The thiazole orange derivative was synthesized according to previously reported procedures (*40*−*42*). The PNA oligomers were purified on reverse phase HPLC and verified by MALDI-TOF mass spectrometry (Applied Biosystems, Voyager DE sSTR) using sinapinic acid as the matrix. ($\mathbf{P_{myc}}$, expected *m*/*z* for $[M + H]^+$, 2460.2; found, 2462.52. $\mathbf{P_{myc}}$**−TO**, expected, 2847.2; found, 2850.73.)

All DNA and PNA concentrations were determined by measuring the absorbance at 260 nm at 85 °C on a Cary 3 Bio spectrophotometer. At high temperatures the bases are assumed to be unstacked, and the extinction coefficient of the oligomer is estimated as the sum of the individual bases. For the DNA oligomers the extinction coefficients were used as reported in the literature (*43*). The PNA extinction coefficients were obtained from Applied Biosystems.

UV Melting Experiments. UV−vis measurements were performed on a Varian Cary 3 spectrophotometer equipped with a thermoelectrically controlled multicell holder. Samples containing DNA and PNA were prepared in a buffer containing 10 mM Tris-HCl (pH 7) and 0.1 mM Na$_2$EDTA. For LiCl thermals, a stock solution of 10 mM Li$_2$EDTA was used. Various concentrations of KCl or LiCl were used. The solutions were heated to 95 °C for 5 min followed by cooling to 15 °C at a rate of 1 °C min^{-1}, equilibrated for 5 min, and then heated back to 95 °C at the same rate. The absorbance at 295 nm was recorded throughout at intervals of 0.5 °C. All figures show the heating curve, which was also used to derive the thermodynamic parameters as described by Marky and Breslauer (*44*). Briefly, the absorbance versus temperature curves were converted into α versus temperature profiles, where α is the fraction of strands that are in a quadruplex form at any given temperature. (In cases where melting curves exhibited pre- and/or post-transitional hyperchromicity, appropriate baselines were subtracted from the data prior to conversion into α-versus-T profiles.) The temperature at $\alpha = 0.5$ was then defined as the melting temperature, T_m, which was used to determine the van't Hoff enthalpy and the equilibrium constant at T_m. Subsequently, this value was extrapolated to $T = 310$ K, using the value of T_m, the van't Hoff enthalpy, and the integrated form of the van't Hoff equation. This enabled determination of the Gibbs free energy using the standard thermodynamic relationship $\Delta G_{310} = -RT \ln K_{310}$ and the enthalpy from $\Delta G_{310} = \Delta H - T\Delta S_{310}$. The heat capacity change was assumed to be zero and hence ΔH was independent of temperature.

Circular Dichroism (CD) Spectropolarimetry. CD measurements were performed on a Jasco J-715 CD spectropolarimeter equipped with a water-circulating temperature controller. Samples were prepared by mixing all components together in 10 mM Tris-HCl (pH 7), 0.1 mM Na$_2$EDTA, and various amounts of KCl. Samples were annealed by heating to 95 °C for 5 min and then slowly cooling to room temperature. All spectra were collected at 37 °C by equilibrating the solutions at this temperature for 10 min prior to recording. Each spectrum represents an average of 10 scans, collected at a rate of 10 nm min^{-1}. The spectra were baseline corrected.

Fluorescence Spectroscopy. Fluorescence emission spectra were collected on a Photon Technology International (PTI) fluorescence system. For the continuous variations experiment, various amounts of **Myc19** and $\mathbf{P_{myc}}$**−TO** were mixed, keeping the total concentration of DNA + PNA fixed at 100 nM. The emission spectra were measured upon excitation of TO at 495 nm. For experiments involving fluorescein-labeled DNA, solutions were prepared by mixing a fixed concentration of the DNA (50 nM) and variable concentrations of $\mathbf{P_{myc}}$. The samples were excited at 475 nm, and emission intensity at 513 nm was used to calculate fraction bound by comparison with the intensity recorded in the presence of a large excess of the PNA. All samples were prepared in buffer containing 10 mM Tris-HCl (pH 7.0), 0.1 mM Na$_2$EDTA, and various KCl concentrations and annealed prior to recording of the spectra. All fluorescence spectra were collected at room temperature.

Surface Plasmon Resonance (SPR) Experiments. SPR measurements were performed by using a Biacore 2000 system with four-channel, streptavidin-coated sensor chips (SA) for all experiments. This chip consists of a gold surface and streptavidin covalently immobilized on a carboxymethylated dextran layer at the surface. 5′-Biotinylated DNA was immobilized on the surface by non-covalent capture to streptavidin. To prepare sensor chips for use, they were conditioned with three consecutive 1 min injections of 1 M NaCl in 50 mM NaOH followed by extensive washing with HEPES buffer (pH 7.4) (0.01 M Hepes, 0.15 M LiCl, 3 mM EDTA, and 50 μL/L surfactant P20). Biotinylated oligonucleotide (25 nM) in coupling buffer (10 mM HEPES, pH 7.4, 3 mM EDTA, and 150 mM LiCl) was heated at 95 °C for 5 min, cooled slowly to room temperature, and then injected at a flow rate of 2 μL/min to achieve long contact times with the surface and to control the amount of the DNA that was immobilized. A high level of **Myc19** DNA, >1000 RU, was used to maximize mass transfer in the competition experiments described below. The $\mathbf{P_{myc}}$ sample was dissolved in water at approximately 1 mM and was then diluted to a working stock solution at 10 μM in the Tris buffer: 10 mM Tris (pH 7.4), 1 mM EDTA, and 100 mM KCl, which was used in all binding determinations. Samples of various PNA concentrations were then prepared in filtered and degassed Tris buffer by serial dilutions from the stock solution.

Solution Competition Analysis. (A) Construction of a Standard Curve. All BIAcore studies were carried out at 25 °C using the $\mathbf{P_{myc}}$ PNA sequence. A range of concentrations of this PNA (0−30 nM) were serially diluted into Tris buffer, and each sample was injected over the **Myc19** DNA biosensor surface at flow rates of 10−30 μL/min in different experiments. The biosensor surface was regenerated after each PNA sample with a 50 mM NaOH wash for 0.5 min to dissociate the PNA−DNA complex. The slope for each $\mathbf{P_{myc}}$ concentration in the linear association region was obtained by averaging the results over a 20 s window beginning 50 s postinjection. Data from the first 50 s of each sensorgram were omitted due to effects at the start of injections, such as sample dispersion and depletion. A plot of the average slopes versus concentrations of $\mathbf{P_{myc}}$ yields a standard curve that can be used to determine the concentration of free $\mathbf{P_{myc}}$ PNA in equilibrium with nonbiotinylated **Myc19** DNA (*45*−*49*). A calibration function was obtained by a linear least-squares fit of the standard curve data. The results are linear over the desired concentration range of 0−30 nM, and the linear function can be used to determine free PNA concentration in the competition experiments described below.

(B) Solution Competition for Determination of Binding Constants. A range of concentrations of nonbiotinylated **Myc19** DNA, determined from preliminary studies to define the competition curve, were serially diluted into Tris buffer and mixed with a constant total concentration of 10−15 nM PNA. Samples were allowed to equilibrate for approximately 2 h at 25 °C and then injected over the calibrated **Myc19**−biosensor surface with flow rates of 10−30 μL/min. Control experiments demonstrated that no significant binding of **Myc19** to the surface is observed in the experimental time range, and the experiment thus provides a measure of the free concentration of $\mathbf{P_{myc}}$. The biosensor surface was regenerated after each sample as described above. Sensorgrams for each solution were obtained, and the slopes of free $\mathbf{P_{myc}}$ binding to the biosensor surface were determined as described above. Free $\mathbf{P_{myc}}$ concentrations, determined from the calibration curve described above, were subtracted from the total PNA concentration in solution for calculation of the bound $\mathbf{P_{myc}}$ concentration and *r*, moles of $\mathbf{P_{myc}}$ bound/total moles of **Myc19** DNA in solution. Equilibrium association constants (K_A) were obtained from the nonlinear least-squares best fit of *r* versus free compound concentration (C_{free})

$$r = n(K_A C_{\text{free}})/(1 + K_A C_{\text{free}}) \tag{1}$$

where $n = 1$ for binding to the short DNA targets and $n = 2$ for binding to two equivalent sites on **Myc19**. (For binding to **Myc19**, a fit to the results with a nonequivalent site model did not provide a significant improvement relative to experimental error.)

Chart 1: Sequences of DNA and PNA Used[a]

Myc19: 5′-AGGGTGGGGAGGGTGGGGA-3′
G_3TG_4: GGGTGGGG
G_4AG_3: GGGGAGGG
P_{myc}: H_2NLys-GGGGAGGG-H
P_{myc}-TO: H_2NLys-GGGGAGGG-TO

[a] Guanines in **Myc19** that participate in quadruplex formation are colored blue and underlined. All DNA sequences are written 5′ to 3′ while the PNA sequences are written C to N terminus.

RESULTS

Formation of an Extremely Stable Hybrid Quadruplex. The target quadruplex-forming sequence described here (**Myc19**) was derived from the NHE III_1 control region of the human oncogene *MYC*. A PNA sequence ($\mathbf{P_{myc}}$) was designed to be perfectly homologous to the central G6−G13 of the DNA sequence **Myc19** (Chart 1). However, it is also possible that $\mathbf{P_{myc}}$ could bind to one or both G_3TG_4 sites in **Myc19** because these sites would still permit formation of hybrid PNA−DNA quadruplexes having three stacked G-tetrads. [We refer to these sites as "G-homologous" because the intervening nucleobases separating the G-tracts on the PNA and DNA strands are not homologous (*28*, *29*).] The PNA was synthesized by standard methods and gave satisfactory HPLC and mass spectral data. In addition, a PNA bearing an N-terminal fluorogenic dye, thiazole orange (TO) (*41*), was synthesized.

$\mathbf{P_{myc}}$ hybridization to **Myc19** was first studied using the TO conjugate of the PNA ($\mathbf{P_{myc}}$−**TO**). TO has been previously used as a fluorescent indicator of PNA binding to its complementary target (*40*). Earlier reports from our laboratory have used this method to probe PNA−DNA and PNA−RNA hybrid quadruplex formation as well (*28, 29*). Hybridization is readily detected with a TO-labeled PNA based on the enhanced fluorescence of the dye upon binding of the PNA to its target. A continuous variation experiment of $\mathbf{P_{myc}}$−**TO**/**Myc19** binding is shown in Figure 1. The apparent formation of a 2:1 complex indicates that the PNA does indeed bind to both of the peripheral G-homologous sites, rather than forming a 1:1 complex by binding to the perfectly homologous central site. This is consistent with prior work from our laboratory, which showed 2:1 hybrid quadruplex formation between a G-rich PNA and an RNA quadruplex target (*28*, *29*). Furthermore, the sharpness of the transition observed in the Job plot indicates a high affinity for the PNA_2−DNA interaction.

UV melting experiments are routinely used to characterize nucleic acid interactions. Quadruplexes in particular give rise to a hypochromic transition when absorbance is measured at 295 nm as a function of temperature (*50*). To determine the relative stabilities of the species involved, we first

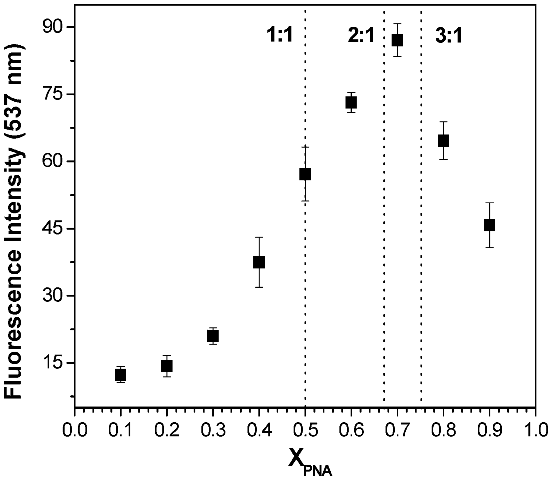

FIGURE 1: Fluorescence Job plot determined for binding of TO-labeled $\mathbf{P}_{\mathbf{myc}}$ to **Myc19**. Total strand concentration = 100 nM. Fluorescence at 537 nm was recorded with excitation at 495 nm. Dotted lines correspond to 1:1, 2:1, and 3:1 stoichiometries. The buffer in this experiment contained 100 mM KCl, 10 mM Tris-HCl (pH 7), and 0.1 mM EDTA.

characterized the UV melting behavior of the **Myc19** sequence by itself. This sequence demonstrated typical hypochromic transitions (Figure 2A), which were dependent on the KCl concentration, as expected of quadruplexes. However, upon addition of $\mathbf{P}_{\mathbf{myc}}$ in a 2-fold excess, the melting temperatures (T_m values) were found to be much higher at each KCl concentration (Figures 2B and 3). In fact, complete transitions for the PNA_2−DNA hybrids could be observed only at KCl concentrations of 2.5 mM or less. (Note that the samples also contained 0.2 mM Na^+ due to the presence of 0.1 mM disodium EDTA in the buffer.) At higher potassium concentrations the melting temperature was beyond the range accessible in these experiments, indicative of the extremely high stability observed previously for PNA_2−RNA (*28*, *29*) and PNA_2−DNA_2 (*27*) hybrid quadruplexes. The melting transitions also exhibited the expected increase with increasing PNA and DNA concentrations, although precipitation occurred at concentrations above 2.5 μM DNA/5.0 μM PNA (see supplementary figure S1 in the Supporting Information).

Figure 3 compares the increase in stability of the DNA and PNA_2−DNA quadruplex as a function of potassium concentration. The slopes of the two lines were found to be quite different as expected. The larger slope for **Myc19** is explained by the fact that K^+ stabilizes DNA quadruplexes not only through coordinating to the carbonyl oxygen on the guanines at the center of the G-tetrad but also by associating with the phosphate backbone and screening the negative charges on the oxygen atoms. In contrast, due to the neutral PNA backbone, the latter effect should be significantly reduced for the PNA_2−DNA quadruplex.

The melting curves were also fitted as described by Marky and Breslauer (*44*) to determine thermodynamic parameters for formation of the **Myc19** quadruplex as well as the PNA_2−DNA hybrid quadruplex (Table 1). The free energy of formation of the PNA_2−DNA quadruplex is greater than that of the DNA quadruplex by ca. 30 kcal mol^{-1} at 0.1 and 1.0 mM KCl. This further emphasizes the fact that a very high affinity complex is formed between **Myc19** and $\mathbf{P}_{\mathbf{myc}}$. In contrast, melting curves recorded in solutions containing LiCl showed much lower melting transitions, although significantly lower hypochromicities were also evident (see supplementary figure S2).

CD spectropolarimetry is usually an excellent method for studying nucleic acid secondary structures. **Myc19** yielded spectra that were characteristic of parallel quadruplexes with a maximum at 260 nm and a minimum at 240 nm (Figure 4), consistent with a prior study (*51*). Interestingly, addition of $\mathbf{P}_{\mathbf{myc}}$ (2 equiv) did not lead to significant changes in the positions of the peaks or the shape of the spectrum at both 10 and 100 mM KCl concentrations. Because the TO fluorescence experiments clearly demonstrate binding of the PNA under these conditions, the CD results indicate that the hybrid PNA−DNA quadruplexes and the **Myc19** DNA quadruplex have similar helical structures. Moreover, the CD spectrum for the 2:1 hybrid quadruplex is similar to those previously reported for PNA_2−RNA and PNA_2−DNA_2 hybrid quadruplexes (*26*−*28*).

Binding to Short DNA Targets. The fact that two PNAs bind to **Myc19** raises the question of whether there is a difference in affinity for the two distinct G-homologous subsequences in **Myc19**, 5′-GGGTGGGG-3′ and 5′-GGGGAGGG-3′ ($\mathbf{G_3TG_4}$ and $\mathbf{G_4AG_3}$, respectively, in Chart 1). We performed UV melting and fluorescence experiments to characterize PNA binding to these truncated targets.

The short DNAs exhibited no hypochromic transitions when monitored at 295 nm in the presence of 1 mM KCl at 2.5 μM DNA strand concentrations, indicating no self-quadruplex formation under these conditions (see supplementary figure S3). However, addition of 1 equiv of $\mathbf{P}_{\mathbf{myc}}$ resulted in a distinct hypochromic transition for $\mathbf{G_3TG_4}$, implying formation of a PNA−DNA quadruplex (Figure 5). The corresponding curve for $\mathbf{G_4AG_3}$ is broader and exhibits a lower hypochromicity, suggesting that $\mathbf{P}_{\mathbf{myc}}$ forms a more stable quadruplex with $\mathbf{G_3TG_4}$ in comparison to $\mathbf{G_4AG_3}$. Considerable hysteresis was also observed in these transitions (data not shown), indicative of slow association kinetics. In contrast, no such hysteresis was observed in the 2:1 $\mathbf{P}_{\mathbf{myc}}$−**Myc19** melting experiments described above. This suggests that higher molecularity complexes (e.g., 2:2 four-stranded quadruplexes, as in ref 16) and/or different structures having complex folds are formed with the short DNA targets.

We also characterized the binding of $\mathbf{P}_{\mathbf{myc}}$ to fluorescein-labeled $\mathbf{G_3TG_4}$ and $\mathbf{G_4AG_3}$, taking advantage of the fact that when the PNA was added to a solution containing a DNA target, the fluorescence was found to be significantly quenched (Figure 6A). Guanines are known to be efficient quenchers of fluorescein emission through a suspected electron-transfer mechanism (*52*, *53*). Because both the fluorescein and the DNA backbone are negatively charged, electrostatic repulsions might prevent the G-rich DNA oligonucleotides from quenching the fluorescence. However, formation of the hybrid PNA−DNA quadruplex reduces the charge density of each G-tetrad by half. (In addition, both termini of the PNA bear positive charges.) This should decrease the electrostatic repulsion with the dye, allowing fluorescein to more closely approach the guanines and enhancing the quenching. Regardless of the origin of the quenching, this phenomenon allows detection of hybridization at low nanomolar concentrations.

Continuous variation experiments with both short strands of DNA labeled with a fluorescein on the 3′ end versus $\mathbf{P}_{\mathbf{myc}}$

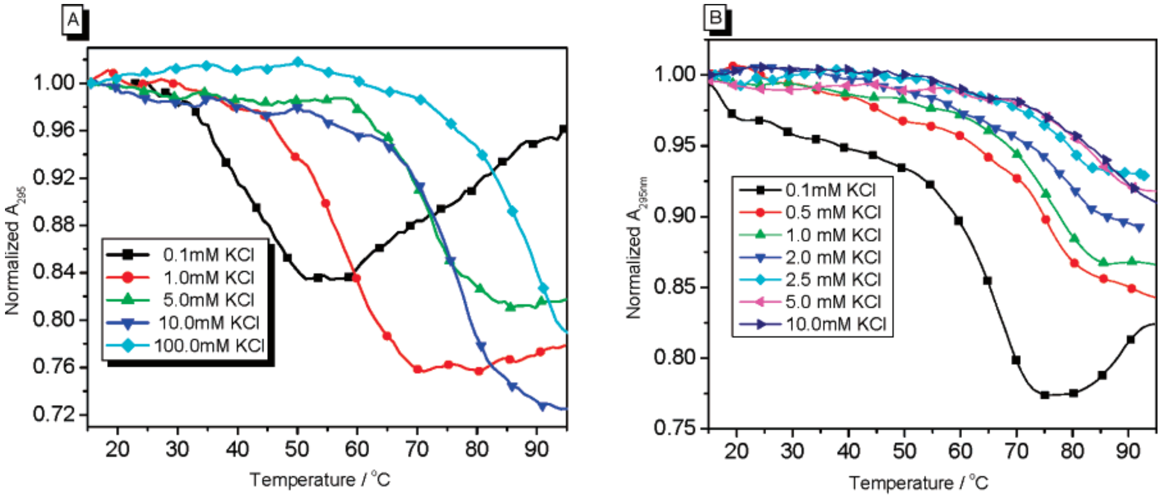

FIGURE 2: UV melting curves monitored at 295 nm demonstrating the potassium-dependent increase in stability of quadruplexes formed by 1.0 μM **Myc19** by itself (A) or in the presence of a 2-fold excess of $\mathbf{P_{myc}}$ (B). The buffer in these experiments contained 10 mM Tris-HCl (pH 7) and 0.1 mM EDTA in addition to the indicated KCl concentration.

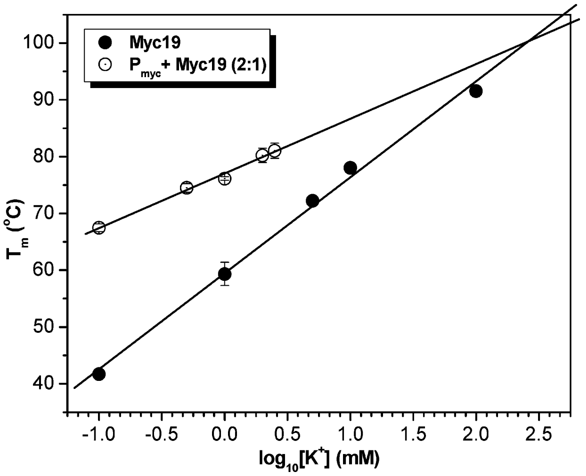

FIGURE 3: Plot of melting temperatures as a function of K^+ concentration for **Myc19** as well as $\mathbf{P_{myc}}$−**Myc19** (2:1) solutions. The T_m values were estimated from the differentials of heating curves shown in Figure 2.

Table 1: Thermodynamic Parameters Derived from Fitting Melting Curves of (A) 1 μM **Myc19** and (B) 1 μM **Myc19** + 2 μM $\mathbf{P_{myc}}$[a]

[KCl] (mM)	ΔG (kcal/mol)	ΔH (kcal/mol)	ΔS (cal/mol)
A. **Myc19** DNA Quadruplex			
0.1	−0.5 ± 0.1	−41.3 ± 6.1	−131.5 ± 19.9
1	−2.7 ± 0.1	−42.9 ± 1.5	−129.9 ± 4.3
5	−5.6 ± 0.3	−56.0 ± 2.9	−162.4 ± 8.3
10	−6.2 ± 0.2	−56.4 ± 1.5	−161.8 ± 4.5
B. $\mathbf{P_{myc}}$−**Myc19** (2:1) Hybrid PNA−DNA Quadruplex			
0.1	−30.6 ± 0.8	−128.9 ± 5.9	−317.5 ± 16.8
0.5	−35.0 ± 1.1	−153.6 ± 0.5	−382.3 ± 3.3
1	−31.2 ± 1.4	−112.3 ± 6.1	−261.8 ± 16.4

[a] All values reported are for 37 °C.

revealed an inflection in the slope at a $\mathbf{P_{myc}}$ mole fraction of approximately 0.5 (see supplementary figure S4) denoting either a 1:1 or a 2:2 binding stoichiometry. Figure 6B compares results from titration of $\mathbf{G_3TG_4}$ and $\mathbf{G_4AG_3}$ against $\mathbf{P_{myc}}$. The EC_{50} value for $\mathbf{G_3TG_4}$ = 25 nM, that is, the minimum possible value given that the DNA concentration for the experiment was 50 nM. Meanwhile, EC_{50} = 113 nM for the binding of $\mathbf{P_{myc}}$ to $\mathbf{G_4AG_3}$, indicating significantly lower affinity of the PNA for the perfectly homologous central eight nucleotides of the **Myc19** DNA target than for the G-homologous flanking target sites.

SPR. SPR experiments are useful for measuring kinetic and equilibrium parameters for binding of small molecules to DNA, but have not been widely used to study PNA−DNA interactions due to difficulties in determining the very high binding constants with significant mass transfer limitations on the reaction kinetics. Figure 7 illustrates the results of a typical SPR experiment in which 25 nM $\mathbf{P_{myc}}$ was flowed over the surface of a chip functionalized with comparable amounts of **Myc19**, $\mathbf{G_3TG_4}$, and $\mathbf{G_4AG_3}$ in different flow cells. Although some valuable information can be obtained from such experiments, such as the observation of greater PNA binding to $\mathbf{G_3TG_4}$ than $\mathbf{G_4AG_3}$, consistent with the fluorescence experiments shown in Figure 6B, the impact of mass transfer on the measurements, the failure to saturate the binding, the incomplete release of the PNA during the dissociation phase, and the 2:1 stoichiometry with **Myc19** limit the quantitative interpretation of the results.

The mass transfer limitation can, however, be used to advantage in a solution competition analysis where the biosensor surface is used simply to measure the free concentration of one reactant (*45*−*49*). To maximize mass transport, a high-density **Myc19**-functionalized SPR chip surface was prepared by immobilizing biotinylated **Myc19** DNA onto a streptavidin-coated carboxymethyldextran surface as described under Experimental Procedures. Typical sensorgrams obtained for different concentrations of $\mathbf{P_{myc}}$ binding to the **Myc19** biosensor surface under mass transport limiting conditions are shown in Figure 8. The slopes and the total response units obtained during the binding phase of the sensorgrams increase proportionately with increase in $\mathbf{P_{myc}}$ concentration, within the range examined (0−30 nM), and a calibration curve of slope versus the solution PNA concentration is shown in the Supporting Information (see supplementary figure S5). On the basis of the maximum response units (RU) observed at the highest PNA concentrations, there are two PNAs bound per **Myc19** DNA, consistent with the fluorescence experiment shown in Figure 1.

Concentrations of nonbiotinylated **Myc19** DNA ranging from 1 to 30 nM were mixed with a fixed concentration of $\mathbf{P_{myc}}$ in Tris buffer for solution competition analysis. PNA

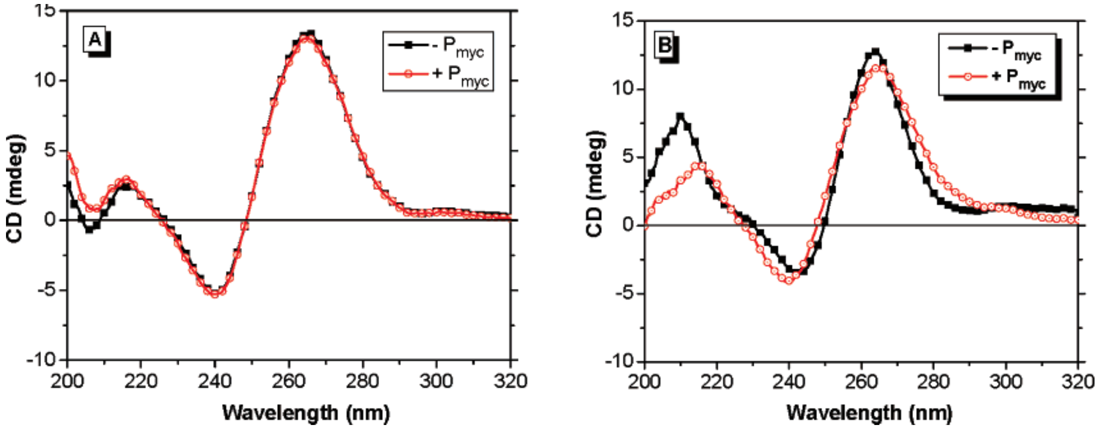

FIGURE 4: CD spectra of 2.5 μM **Myc19** in the absence and presence of 5.0 μM $\mathbf{P_{myc}}$ in (A) 100 mM KCl or (B) 10 mM KCl. All spectra were recorded in 10 mM Tris-HCl (pH 7.0) and 0.1 mM EDTA.

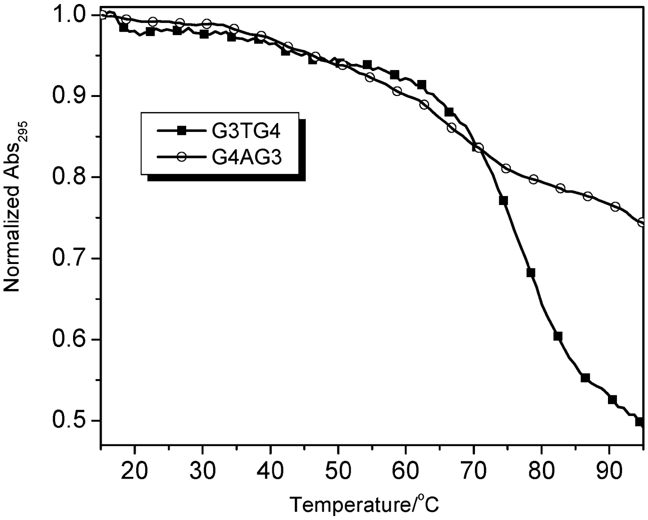

FIGURE 5: UV melting curves recorded at 295 nm for $\mathbf{P_{myc}}$ versus $\mathbf{G_4AG_3}$ and $\mathbf{G_3TG_4}$ DNA sequences. The concentrations of the DNA or PNA strands were 2.5 μM, and the buffer contained 1 mM KCl.

concentrations of 10 or 15 nM were used in separate experiments and gave equivalent equilibrium constants within experimental error. The solutions were equilibrated for 2 h at 25 °C, and then samples were individually injected over the calibrated high-density **Myc19**−biosensor surface to generate a series of binding sensorgrams (Figure 9). Control experiments verified that the nonbiotinylated **Myc19** DNA does not bind to the immobilized **Myc19** DNA in the time span of the experiments (data not shown). As the concentration of **Myc19** DNA in solution increases, the amount of free $\mathbf{P_{myc}}$ in solution available for binding to the biosensor surface decreases. The slopes of the sensorgrams in the linear association region are proportional to the concentration of free $\mathbf{P_{myc}}$ when the experiment is conducted under mass transport limited conditions.

The calculated free $\mathbf{P_{myc}}$ concentration, from the linear fit to the standard curve (Experimental Procedures), is plotted versus r in Figure 10, and the best-fit curve to the data was determined by using a two equivalent site binding model (eq 1). Nonlinear least-squares fitting of the results in Figure 10 gives $K_a = (2.0 \pm 0.2) \times 10^8$ M^{-1} or $K_d = 5.0$ nM. It is important to emphasize that this value corresponds to binding of the $\mathbf{P_{myc}}$ to the **Myc19** DNA in solution; the SPR signal is used only to determine the free PNA concentration. Using different $\mathbf{P_{myc}}$ concentrations and flow rates in the competition experiment (10 or 15 nM $\mathbf{P_{myc}}$ and 10 or 30 μL/min) gave K_a values of $(2.0 \pm 0.2) \times 10^8$ M^{-1} in all cases. $\mathbf{P_{myc}}$ concentrations below 10 nM did not give sufficient signal to obtain a full binding curve, and the best results were obtained at 15nM $\mathbf{P_{myc}}$. The Gibbs energy for binding of the two $\mathbf{P_{myc}}$ strands to the **Myc19** model DNA is $\Delta G = -2RT \ln K_a = -22.9$ kcal/mol, which is in the range of strong protein−DNA complexes. The lower value determined by SPR compared with the melting curve analysis ($\Delta G = -30$ to 35 kcal/mol) likely reflects the difference in ionic strength for the two experiments because the higher KCl concentration used in SPR will stabilize the **Myc19** quadruplex more than the PNA_2−DNA hybrid, as suggested by the ionic strength dependence of the T_m for the two quadruplexes (Figure 3).

The experiment was next repeated using the short DNA strands as competitors. Preliminary experiments demonstrated no binding of the competitor DNAs with the immobilized **Myc19** (data not shown). Thus, the immobilized and competitor strands need not be the same in order to perform the SPR competition assay. As shown in Figure 10, $\mathbf{P_{myc}}$ exhibits 2.4-fold higher affinity for $\mathbf{G_3TG_4}$ versus $\mathbf{G_4AG_3}$: $K_a = 1.4 \times 10^8$ M^{-1} and 0.59×10^8 M^{-1}, respectively. These results are consistent with the UV melting and fluorescence experiments shown in Figures 6 and 7.

DISCUSSION

DNA sequences that are able to form quadruplexes (QFSs) are prominent in many biological contexts such as promoter regions of genes and telomeres of the chromosomes. In this paper we report the high-affinity binding of a guanine-rich PNA to a DNA QFS derived from the promoter region of the human proto-oncogene *MYC*.

Binding Affinity. As observed for other PNA−DNA and PNA−RNA hybrid quadruplexes, very high thermodynamic stabilities were measured from UV melting curves for the $(\mathbf{P_{myc}})_2$−**Myc19** quadruplex. T_m values were found to be dependent on the concentration of KCl as well as the type of ion present, characteristic of quadruplex formation. However, the hybrid complexes were found to be so stable that complete melting transitions could be obtained only at low potassium concentrations. The high stability of these complexes is further reflected in the free energy values determined from the melting curves ($\Delta G = -30$ to 35 kcal

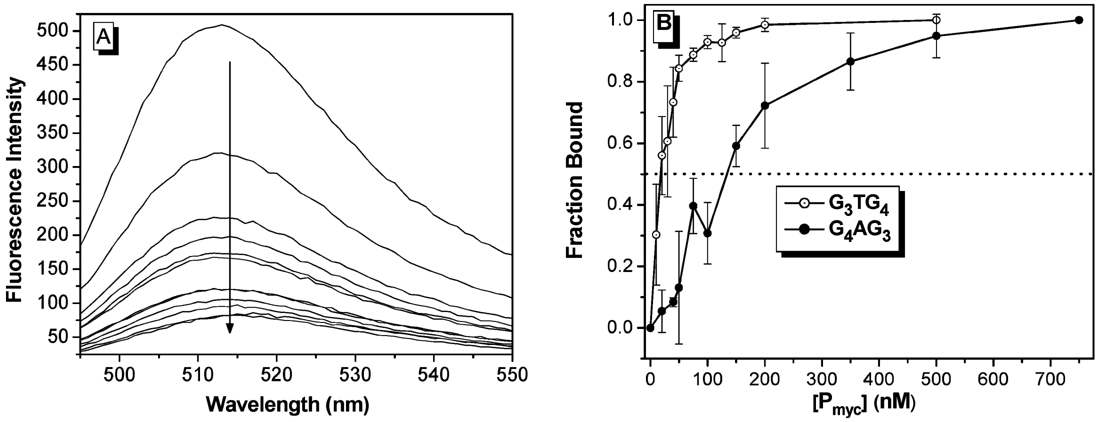

FIGURE 6: (A) Representative fluorescence spectra showing quenching of fluorescence from 50 nM **G$_3$TG$_4$** conjugated to a fluorescein upon successive additions of **P$_{myc}$**. Arrow indicates increasing PNA concentration. (B) Plot of fraction bound versus added PNA for the two short DNA strands. Dotted line shows 50% bound DNA. The experiments in the figure were carried out in buffer containing 150 mM KCl.

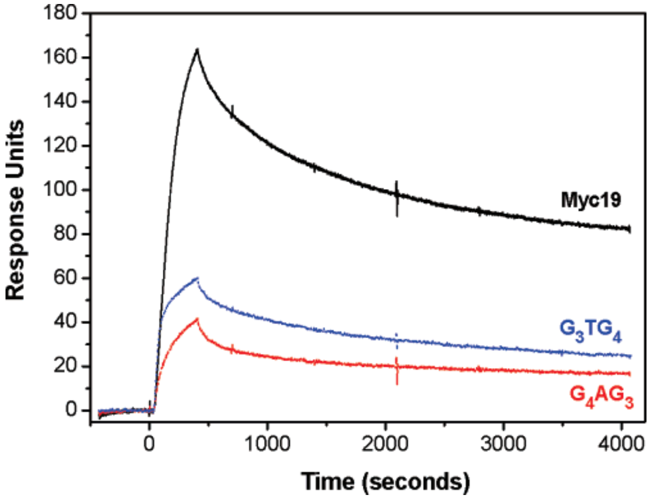

FIGURE 7: SPR experiment in which 25 nM **P$_{myc}$** PNA was flowed over chip containing comparable amounts of biotinylated **Myc19**, **G$_3$TG$_4$**, and **G$_4$AG$_3$**, immobilized on a streptavidin-coated chip. Buffer contained 10 mM HEPES (pH 7.4), 150 mM KCl, and 3 mM EDTA.

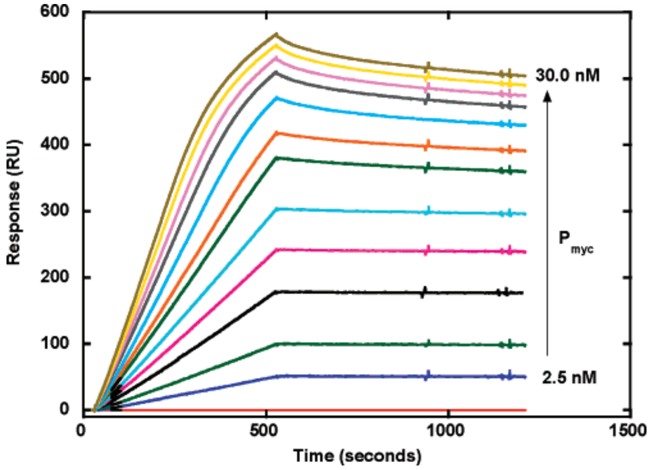

FIGURE 8: Sensorgrams for the direct interaction of **P$_{myc}$** with immobilized **Myc19**. The initial region of the association reaction is mass transport limited, and this is where the slopes are determined to prepare the calibration curve. At 600 s, the flow of **P$_{myc}$** is stopped, and buffer flow is restarted to monitor the dissociation reaction. Very slow dissociation, mass transfer, and complex association kinetics limit the quantitative analysis of these direct binding curves. The concentrations of **P$_{myc}$** increase from 2.5 nM in the lowest sensorgram to 30 nM in the top sensorgram, and the concentration intervals between plots are 2.5 nM. The calibration curve prepared from this experiment is given in the Supporting Information.

mol^{-1}; Table 1) at lower potassium concentrations as well as the SPR experiments at higher potassium ($\Delta G = -22.9$ kcal/mol). The formation of a ternary complex leads to a greater loss in entropy than for the DNA quadruplex itself. The new structure comprising two PNA−DNA quadruplexes, though, should be favored enthalpically as the numbers of hydrogen bonds and stacking interactions are twice those of the DNA quadruplex. (It is also possible that the two hybrid quadruplexes stack on one another coaxially.) In addition, the electrostatic repulsions inherent in a pure DNA quadruplex are relaxed when two of the four backbones are neutral PNA. This effect is reflected in the weaker dependence of the T_m on the potassium concentration shown in Figure 3.

SPR experiments allowed determination of the equilibrium binding constant for quadruplex formation. Attempts at direct kinetics and thermodynamics characterization of the **Myc19**−**P$_{myc}$** interaction were not successful due to the multiple stoichiometry of the reaction, its kinetic complexity, with some required unfolding of **Myc19** for binding, and significant mass transfer. The mass transfer limitation of reaction kinetics was, however, turned to advantage in a solution competition experiment. On a high-density **Myc19** surface, **P$_{myc}$** initially binds in a completely mass transfer limited process at low concentrations, and the signal produced on interaction of **P$_{myc}$** with the **Myc19** surface is directly related to the concentration of free **P$_{myc}$** in solution. From the known total concentration of **P$_{myc}$** in solution, the bound concentration can be determined at any added concentration of **Myc19** to provide a complete binding curve as shown in Figure 10. The RU values at high ratios of **P$_{myc}$** to **Myc19** are only consistent with a 2:1 stoichiometry for the complex. With the binding curve and stoichiometry, a fit to the curve was obtained with a 2:1 equivalent binding site model (Figure 10), and the value of K_a, the microscopic binding constant for each site, obtained from the fit is 2.0×10^8 M^{-1}. Similar experiments with DNA models for the two possible PNA binding sites in **Myc19** gave values that are lower by a factor of 2−4. It should be emphasized that these are binding constants in solution, and the biosensor surface is used only to determine free PNA concentration in equilibrium with

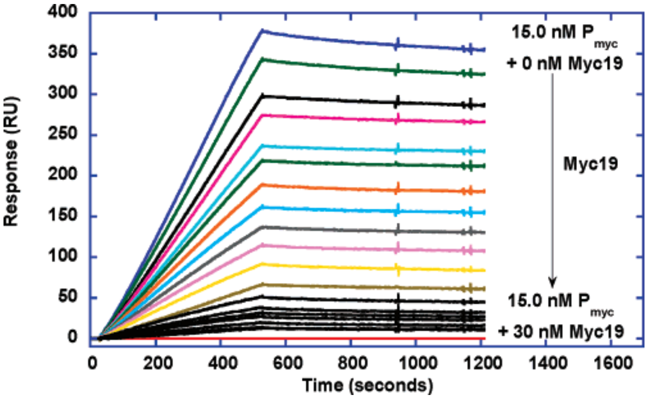

FIGURE 9: Sensorgrams for the solution competition experiment between $\mathbf{P_{myc}}$ and **Myc19**. As in Figure 8, the slopes in the initial, mass transport limited region were determined to calculate the free concentration of $\mathbf{P_{myc}}$ in equilibrium with **Myc19**. The total $\mathbf{P_{myc}}$ concentration is constant at 15 nM, whereas the **Myc19** concentration increases from 0 nM in the top curve to 30 nM in the bottom curve. As the **Myc19** concentration is increased, the concentration of free $\mathbf{P_{myc}}$ decreases significantly as a result of solution complex formation.

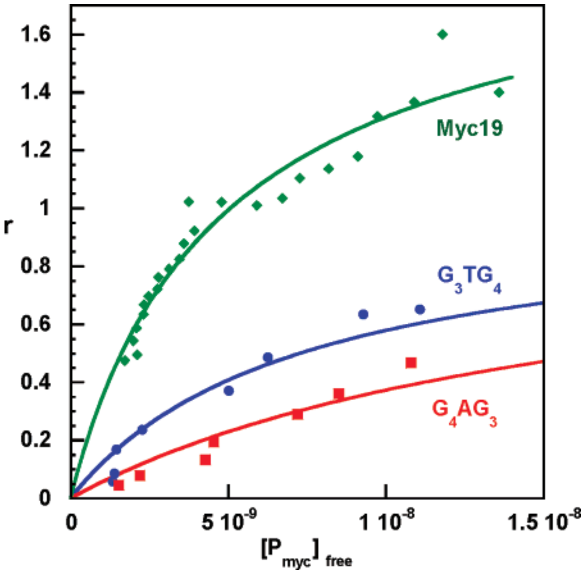

FIGURE 10: Plots of *r* versus the free $\mathbf{P_{myc}}$ concentration, determined as in Figure 9. The **Myc19** results represent an overlay from two separate experiments and were fit with a two-equivalent site binding model as described under Methods. Results for a 1:1 binding model for the shorter DNA binding sequences, determined as for **Myc19**, are also shown. *K* values determined in this manner are **Myc19**, $K_a = 2.0 \times 10^8\ \mathrm{M}^{-1}$; $\mathbf{G_3TG_4}$, $K_a = 1.4 \times 10^8\ \mathrm{M}^{-1}$; and $\mathbf{G_4AG_3}$, $K_a = 0.59 \times 10^8\ \mathrm{M}^{-1}$.

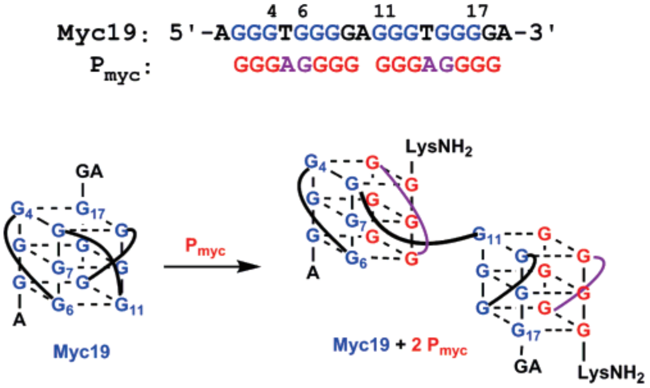

FIGURE 11: Structural model of a 2:1 $\mathbf{P_{myc}}$−**Myc19** complex.

Myc19 in solution. This method obviously is quite useful for providing equilibrium information for complex reactions such as that for **Myc19**−$\mathbf{P_{myc}}$, and the results illustrate the very large affinity that can be obtained in a homologous interaction of a short PNA with a DNA quadruplex-forming G-strand.

Sequence-Dependence of Hybrid Quadruplex Formation. Our prior work with RNA quadruplexes and the present results with **Myc19** demonstrate that G-rich PNA can bind to G-rich RNA or DNA and form hybrid quadruplexes, even without being perfectly homologous. This is evidenced by the 2:1 binding stoichiometries as well as the experiments with the short oligonucleotides, $\mathbf{G_4AG_3}$ and $\mathbf{G_3TG_4}$. The competition SPR results shown in Figure 10 indicate that the PNA binds $\mathbf{G_3TG_4}$ with 2.4-fold higher affinity than $\mathbf{G_4AG_3}$, whereas the fluorescence quenching experiments suggest somewhat higher selectivity (ca. 4−5-fold) for $\mathbf{G_3TG_4}$.

Binding Model. Continuous variation experiments of **Myc19** versus $\mathbf{P_{myc}}$ as well as SPR experiments revealed 2:1 binding of the PNA to the DNA target, similar to what we observed previously for a G-rich PNA and an RNA that folded into an intramolecular quadruplex (*28*, *29*). It is likely that $\mathbf{P_{myc}}$ invades the **Myc19** quadruplex to form two three-tetrad PNA−DNA hybrid quadruplexes such as shown in the schematic in Figure 11.

There are numerous possible configurations for the ternary complex, distinguished by (a) which G-tracts in the DNA are bound by each PNA, (b) the PNA orientation, and (c) the conformation of the DNA and PNA loops. The model shown in Figure 11 addresses each of these questions and is based on the following considerations.

G-Tract Selection. In theory, two $\mathbf{P_{myc}}$ molecules could bind to **Myc19** in two different ways with respect to the specific G-tracts in the target that are recognized by each PNA. First, one PNA could bind to tracts 1 and 2 (i.e., G_2−G_4 and G_7−G_9), whereas the second PNA binds to tracts 3 and 4 (i.e., G_{11}−G_{13} and G_{16}−G_{18}). Alternatively, one PNA could bind to tracts 2 and 3 and the second PNA to tracts 1 and 4. The experiments involving the short DNA targets indicate a modest preference for the $\mathbf{G_3TG_4}$ subsequence over $\mathbf{G_4AG_3}$ (Figures 6B and 10), favoring the model shown in Figure 11.

PNA Orientation. The CD spectra shown in Figure 4 are similar to that recorded for the hybrid quadruplex formed between the homologous DNA and PNA strands having the sequence $\mathbf{G_4T_4G_4}$ (*27*). In that case, FRET experiments demonstrated that the 3′ terminus of the DNA aligns with the C terminus of the PNA. Thus, Figure 11 orients the two PNA strands such that their C-terminal lysine residues are aligned with the 3′ terminus of the DNA. (Note that other isomers are possible, e.g., where the C-terminal G of the PNA hybridized to tracts 1 and 2 is directly H-bonded to G_4 of **Myc19** instead of G_9.)

Loop Conformations. The proposed model requires minimal structural perturbation and should allow all of the DNA guanines to remain in an *anti* conformation (*54*, *55*), which is consistent with the similarity between the CD spectra for the hybrid PNA−DNA and pure DNA quadruplexes (Figure 4). Moreover, the imposition of double-chain reversal loops

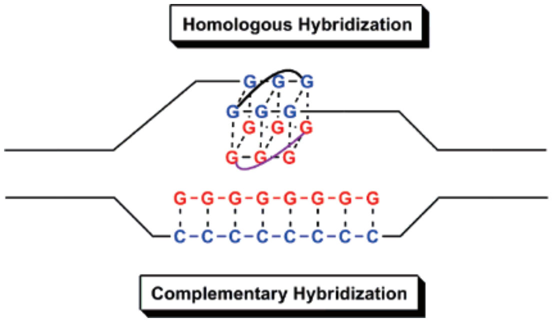

FIGURE 12: Guanine-rich PNA is capable of binding both strands of DNA at homologous/complementary site through simultaneous quadruplex and duplex formation.

on both the PNA and DNA is required to give the proper strand orientation.

Implications for Biological Applications. There is great interest in developing G-quadruplex-binding compounds due to the likely role played by quadruplexes in regulating gene expression, not only at the transcriptional level (*5*−*8*, *37*, *56*) but also in splicing of pre-mRNA (*12*, *13*) and translation (*57*). Most efforts to date have focused on small molecules that are designed to bind selectively to quadruplex DNA over duplex DNA (*20*−*23*, *58*−*61*), a necessary feature for targeting genomic quadruplexes. Small molecules can function in several ways, including (i) binding to pre-existing quadruplex, (ii) inducing quadruplex formation in a non-quadruplex region, and (iii) inducing refolding of a quadruplex into an alternative conformation. The resulting complex would then serve to regulate gene expression, perhaps through inhibiting binding of a transcription factor to a promoter, although other mechanisms are possible.

There are two ways in which PNA (or other DNA-like compounds) can bind to quadruplex-forming sequences: complementary strands bind to yield hybrid duplexes (*25*, *26*), whereas homologous strands bind to form hybrid quadruplexes (*27*−*29*). In either case, the resulting hybrid has a very different structure that should not be recognized by proteins that normally bind to the endogenous quadruplex. Moreover, given the high affinity of both complementary and homologous PNA for DNA, it should be difficult for transcription factor proteins to compete with a bound PNA.

Although both complementary and homologous PNAs could be used to target quadruplex-forming sequences in genomic DNA, homologous PNAs offer a potential advantage. As shown in Figure 12, the G-rich PNA can bind to the homologous DNA strand to form a hybrid quadruplex. In addition, the G-rich PNA is automatically complementary to the other DNA strand. Whereas unmodified PNAs have difficulty invading GC-rich sequences of DNA to form hybrid duplexes, hybrid quadruplex formation on the other strand should help to make the C-rich strand accessible for binding by the PNA (and vice versa). Thus, a single PNA has the potential to bind to both strands of DNA at the same site. If realized, this binding mode would complement the double-duplex invasion strategy that relies on pseudocomplementary PNA strands and is most effective at AT-rich sequences (*62*).

A key aspect of designing compounds that regulate gene expression at the transcriptional level is optimizing the selectivity of the compound so that the resulting phenotype can be attributed to activation or inhibition of a specific gene. Both oligomeric compounds such as PNAs and small molecules should therefore bind preferentially to one quadruplex (or quadruplex-forming sequence) over all others. This will be quite challenging to achieve, but the preference for binding of $\mathbf{P_{myc}}$ to 5′-G_3TG_4-3′ versus 5′-G_4AG_3-3′ is encouraging.

An additional level of selectivity is required for both small molecules and PNAs. Small molecules must avoid binding nonselectively to genomic duplex DNA, which will always be present in large excess relative to a genomic quadruplex target. Meanwhile, G-rich PNAs must also avoid cytosine-rich RNAs inside the cell that could intercept the PNA by forming a hybrid duplex. Such RNAs could not only decrease the potency of the PNA but also lead to side effects if the bound PNA prevents the RNA from performing its cellular function. Backbone modifications of the PNA could assist in reducing binding to complementary competitors without compromising hybrid quadruplex formation (*63*, *64*). Experiments are in progress to test this hypothesis.

In conclusion, the results presented here demonstrate high-affinity binding of a guanine-rich PNA to a DNA G-quadruplex modeled on a *MYC* transcriptional regulatory element. The PNA invades the DNA quadruplex to form a very stable PNA_2−DNA hybrid quadruplex structure. Ongoing work is directed toward understanding the sequence selectivity of quadruplex formation as well as probing the biochemical effects of homologous hybridization.

ACKNOWLEDGMENT

We thank Dr. Baburao Renikuntla for synthesis of the thiazole orange derivative and Rebecca Barnett for expert technical assistance. Mass spectra were recorded in the Center for Molecular Analysis at Carnegie Mellon, supported by NSF CHE-9808188 and DBI-9729351.

SUPPORTING INFORMATION AVAILABLE

Supplementary figures S1−S5. This material is available free of charge via the Internet at http://pubs.acs.org.

REFERENCES

1. Davis, J. T. (2004) G-Quartets 40 years later: From 5′-GMP to molecular biology and supramolecular biology, *Angew. Chem., Int. Ed. 43*, 668−698.
2. Simonsson, T. (2001) G-Quadruplex DNA structures−Variations on a theme, *Biol. Chem. 382*, 621−628.
3. Sen, D., and Gilbert, W. (1990) A sodium−potassium switch in the formation of four-stranded G4-DNA, *Nature 344*, 410−414.
4. Sen, D., and Gilbert, W. (1988) Formation of parallel four-stranded complexes by guanine-rich motifs in DNA and its implications for meiosis, *Nature 334*, 364−366.
5. De Armond, R., Wood, S., Sun, D., Hurley, L. H., and Ebbinghaus, S. W. (2005) Evidence for the presence of a guanine quadruplex forming region within a polypurine tract of the hypoxia inducible factor 1R promoter, *Biochemistry 44*, 16341−16350.
6. Dai, J., Dexheimer, T. S., Chen, D., Carver, M., Ambrus, A., Jones, R. A., and Yang, D. (2006) An intramolecular G-quadruplex structure with mixed parallel/antiparallel G-strands formed in the human *BCL-2* promoter region in solution, *J. Am. Chem. Soc. 128*, 1096−1098.
7. Fernando, H., Reszka, A. P., Huppert, J., Ladame, S., Rankin, S., Venkitaraman, A. R., Neidle, S., and Balasubramanian, S (2006) A conserved quadruplex motif located in a transcription activation site of human *c-kit* oncogene, *Biochemistry 45*, 7854−7860.
8. Simonsson, T., Pecinka, P., and Kubista, M. (1998) DNA tetraplex formation in the control region of c-myc, *Nucleic Acids Res. 26*, 1167−1172.

9. Mergny, J. L., Riou, J. F., Maillet, P., Teulade-Fichou, M. P., and Gilson, E. (2002) Natural and pharmacological regulation of telomerase, *Nucleic Acids Res. 30*, 839−865.
10. Neidle, S., and Parkinson, G. (2002) Telomere maintenance as a target for anticancer drug discovery, *Nat. Rev. Drug Discov. 1*, 383−393.
11. Hurley, L. H. (2002) DNA and its associated processes as targets for cancer, *Nat. Rev. Cancer 2*, 188−200.
12. Kostadinov, R., Malhotra, N., Viotti, M., Shine, R., D'Antonio, L., and Bagga, P. (2006) GRSDB: a database of quadruplex forming G-rich sequences in alternatively processed mammalian pre-mRNA sequences, *Nucleic Acids Res. 34*, D119−D124.
13. Gomez, D., Lemarteleur, T., Lacroix, L., Mailliet, P., Mergny, J. L., and Riou, J. F. (2004) Telomerase downregulation induced by the G-qaudruplex ligand 12459 in A549 cells is mediated by hTERT RNA alternative splicing, *Nucleic Acids Res. 32*, 371−379.
14. Todd, A. K., Johnston, M., and Neidle, S. (2005) Highly prevalent putative quadruplex sequence motifs in human DNA, *Nucleic Acids Res. 33*, 2901−2907.
15. Huppert, J. L., and Balasubramanian, S. (2005) Prevalence of quadruplexes in the human genome, *Nucleic Acids Res. 33*, 2908−2916.
16. Huppert, J. L., and Balasubramanian, S. (2007) G-quadruplexes in promoters throughout the human genome, *Nucleic Acids Res. 35*, 406−413.
17. Paeschke, K., Simonsson, T., Postberg, J., Rhodes, D., and Lipps, H. J. (2005) Telomere end-binding proteins control the formation of G-quadruplex DNA structures in vivo, *Nat. Struct. Mol. Biol. 12*, 847−854.
18. Incles, C. M., Schultes, S., and Neidle, S. (2003) Telomerase inhibitors in cancer therapy: current status and future directions, *Curr. Opin. Invest. Drugs 4*, 675−685.
19. Grand, C. L., Han, H., Muñoz, R. M., Weitman, S., Von Hoff, D. D., Hurley, L. H., and Bearss, D. J. (2002) The Cationic porphyrin TMPyP4 down-regulates c-MYC and human telomerase reverse transcriptase expression and inhibits tumor growth *in vivo*, *Mol. Cancer Ther. 1*, 565−573.
20. Olaussen, K. A., Dubrana, K., Domont, J., Spano, J. P., Sabatier, L., and Soria, J. C. (2006) Telomeres and telomerases as targets for anticancer drug developments, *Crit. Rev. Oncol. Hematol. 57*, 191−214.
21. Phan, A. T., Kuryavyi, V., Gaw, Y. H., and Patel, D. J. (2005) Small molecule interaction with a five-guanine-tract G-quadruplex structure from the human *MYC* promoter, *Nat. Chem. Biol. 1*, 167−173.
22. Saretzki, G. (2003) Telomerase inhibition as cancer therapy, *Cancer Lett. 194*, 209−219.
23. White, E. W., Tanious, F., Ismail, M. A., Reszka, A. P., Neidle, S., Boykin, D. W., and Wilson, W. D. (2007) Structure-specific recognition of quadruplex DNA by organic cations: Influence of shape, substituents and charge, *Biophys. Chem. 126*, 140−153.
24. Chen, Q., Kuntz, I. D., and Shafer, R. H. (1996) Spectroscopic recognition of guanine dimeric hairpin quadruplexes by a carbocyanine dye, *Proc. Natl. Acad. Sci. U.S.A. 93*, 2635−2639.
25. Datta, B., and Armitage, B. A. (2001) Hybridization of PNA to structured DNA targets: quadruplex invasion and the overhang effect, *J. Am. Chem. Soc. 123*, 9612−9619.
26. Green, J. J., Ying, L., Klenerman, D., and Balasubramanian, S. (2003) Kinetics of unfolding the human telomeric DNA quadruplex using a PNA trap, *J. Am. Chem. Soc. 125*, 3763−3767.
27. Datta, B., Schmitt, C., and Armitage, B. A. (2003) Formation of a PNA_2−DNA_2 hybrid quadruplex, *J. Am. Chem. Soc. 125*, 4111−4118.
28. Marin, V. L., and Armitage, B. A. (2005) RNA guanine quadruplex invasion by complementary and homologous PNA probes, *J. Am. Chem. Soc. 127*, 8032−8033.
29. Marin, V. L., and Armitage, B. A. (2006) Hybridization of complementary and homologous peptide nucleic acid oligomers to a guanine quadruplex-forming RNA, *Biochemistry 45*, 1745−1754.
30. Cooney, M., Czernuszewicz, G., Postel, E. H., Flint, S. J., and Hogan, M. E. (1988) Site-specific oligonucleotide binding represses transcription of the human *c-myc* gene *in vitro*, *Science 241*, 456−459.
31. Siebenlist, U., Hennighhausen, L., Battey, J., and Leder, P. (1984) Chromatin structure and protein binding in the putative regulatory region of the, *c-myc* gene in Burkitt lymphoma, *Cell 37*, 381−391.
32. Pelengaris, S., Rudolph, B., and Littlewood, T. (2000) Action of Myc, *in vivo*—proliferation and apoptosis. *Curr. Opin. Genet. Dev. 10*, 100−105.
33. Sears, R. C. (2004) The life cycle of C-myc: from synthesis to degradation, *Cell Cycle 3*, 1133−1137.
34. Pelengaris, S., Khan, M., and Evan, G. (2002) c-Myc: more than just a matter of life and death, *Nat. Rev. Cancer 2*, 764−776.
35. Prochownik, E. V. (2004) c-Myc as a therapeutic target in cancer, *Expert Rev. Aanticancer Ther. 4*, 289−302.
36. Secombe, J., Pierce, S. B., and Eisenman, R. N. (2004) Myc: A weapon of mass destruction, *Cell 117*, 153−156.
37. Siddiqui-Jain, A., Grand, C. L., Bearss, D. J., and Hurley, L. H. (2002) Direct evidence for a G-quadruplex in a promoter region and its targeting with a small molecule to repress *c-Myc* transcription, *Proc. Natl. Acad. Sci. U.S.A. 99*, 11593−11598.
38. Koch, T. (2004) in *Peptide Nucleic Acids: Protocols and Applications* (Nielsen, P. E., Ed.) pp 37−60, Horizon Bioscience, Norfolk, U.K.
39. Christensen, L., Fitzpatrick, R., Gildea, B., Petersen, K. H., Hansen, H. F., Koch, T., Egholm, M., Buchardt, O., Nielsen, Coull, P. E. J., and Berg, R. H. (1995) Solid-phase synthesis of peptide nucleic acids, *J. Pept. Sci. 1*, 175−183.
40. Zhou, X.-f., Peng, Z.-h., Geise, J., Peng, B.-x., Li, Z.-x., Yan, M., Domisse, R., Carieer, R., and Claeys, M. (1995) Blue sensitizing dyes: Synthesis, spectroscopy, and performance in photographic emulsions, *J. Imaging Sci. Technol. 39*, 244−252.
41. Svanvik, N., Westman, G., Wang, D., and Kubista, M. (2000) Light-up probes: thiazole orange-conjugated peptide nucleic acid for detection of target nucleic acid in homogeneous solution, *Anal. Biochem. 281*, 26−35.
42. Lee, L. G., Chen, C. H., and Chiu, L. A. (1986) Thiazole orange: a new dye for reticulocyte analysis, *Cytometry 7*, 508−517.
43. Dawson, R. M. C., Elliott, D. C., Elliott, W. H., and Jones, K. M. (1986) in *Data for Biochemical Research*, pp 103−114, Oxford University Press, New York.
44. Marky, L. A., and Breslauer, K. J. (1987) Calculating thermodynamic data for transitions of any molecularity from equilibrium melting curves, *Biopolymers 26*, 1601−1620.
45. Karlsson, R., Fagerstam, L., Nilshans, H., and Persson, B. (1993) Analysis of active antibody concentration. Separation of affinity and concentration parameters, *J. Immunol. Methods 166*, 75−84.
46. Karlsson, R. (1994) Real-time competitive kinetic analysis of interactions between low-molecular-weight ligands in solution and surface immobilized receptors, *Anal. Biochem. 221*, 142−151.
47. Nieba, L., Krebber, A., and Pluckthun, A. (1996) Competition BIAcore for measuring true affinities: large differences from values determined from binding kinetics, *Anal. Biochem. 234*, 155−165.
48. Adamczyk, M., Moore, J. A., and Yu, Z. (2000) Application of surface plasmon resonance towards studies of low-molecular-weight antigen-antibody binding interactions, *Methods 20*, 319−328.
49. *BIAevaluation Software Handbook* (1997) BIAcore, Inc., Piscataway, NJ.
50. Mergny, J. L., Phan, A. T., and Lacroix, L. (1998) Following G-quartet formation by UV-spectroscopy, *FEBS Lett. 435*, 74−78.
51. Seenisamy, J., Rezler, E. M., Powell, T. J., Tye, D., Gokhale, V., Joshi, C. S., Siddiqui-Jain, A., and Hurley, L. H. (2004) The dynamic character of the G-quadruplex element in the *c-Myc* promoter and modification by TMPyP4, *J. Am. Chem. Soc. 126*, 8702−8709.
52. Cardullo, R. A., Sudhir, A., Flores, C., Zamenick, P. C., and Wolf, D. E. (1988) Detection of nucleic acid hybridization by nonradiative fluorescence resonance energy transfer, *Proc. Natl. Acad. Sci. U.S.A. 85*, 8790−8794.
53. Walter, N. G., and Burke, J. M. (1997) Real-time monitoring of hairpin ribozyme kinetics through base-specific quenching of fluorescein-labeled substrates, *RNA 3*, 392−404.
54. Phan, A. T., Modi, Y. S., and Patel, D. J. (2004) Propeller-type parallel-stranded G-quadruplex in the human *c-myc* promoter, *J. Am. Chem. Soc. 126*, 8710−8716.
55. Ambrus, A., Chen, D., Dai, J., Jones, R. A., and Yang, D. (2005) Solution structure of the biologically relevant G-quadruplex element in the human c-MYC promoter. Implications for G-quadruplex stabilization, *Biochemistry 44*, 2048−2058.
56. Rankin, S., Reszka, A. P., Huppert, J., Zloh, M., Parkinson, G. N., Todd, A. K., Ladame, S., Balasubramanian, S., and Neidle,

S. (2005) Putative DNA quadruplex formation within the human *c-kit* oncogene, *J. Am. Chem. Soc 127*, 10584−10589.

57. Kumari, S., Bugaut, A., Huppert, J., and Balasubramanian, S. (2007) An RNA G quadruplex in the 5′UTR of the *NRAS* proto-oncogene modulates translation, *Nat. Chem. Biol. 3*, 218−221.
58. Rezler, E. M., Bearss, D. J., and Hurley, L. H. (2003) Telomere inhibition and telomere disruption as processes for drug targeting, *Annu. Rev. Pharmocol. Toxicol. 43*, 359−379.
59. Mergny, J. L., Riou, J. F., Mailliet, P., Teulade-Fichou, M. P., and Gilson, E. (2002) Natural and pharmacological regulation of telomerase, *Nucleic Acids Res. 30*, 839−865.
60. Cuesta, J., Read, M. A., and Neidle, S. (2003) The design of G-quadruplex ligands as telomerase inhibitors, *Mini Rev. Med. Chem. 3*, 11−21.
61. Seenisamy, J., Bashyam, S., Gokhale, V., Vankayalapati, H., Sun, D., Siddiqui-Jain, Streiner, A., Shin-ya, N., White, K., Wilson, E. W. D., and Hurley, L. H. (2005) Design and synthesis of an expanded porphyrin that has selectivity for the c-Myc G-quadruplex structure, *J. Am. Chem. Soc 127*, 2944−2959.
62. Lohse, J., Dahl, O., and Nielsen, P. E. (1999) Double duplex invasion by peptide nucleic acid: a general principle for sequence-specific targeting of double-stranded DNA, *Proc. Natl. Acad. Sci. U.S.A. 96*, 11804−11808.
63. Englund, E. A., Xu, Q., Witschi, M. A., and Appella, D. H. (2006) PNA−DNA duplexes, triplexes, and quadruplexes are stabilized with *trans*-cyclopentane units, *J. Am. Chem. Soc. 128*, 16456−16457.
64. Dragulescu-Andrasi, A., Rapireddy, S., Frezza, B. M., Gayathri, C., Gil, R. R., and Ly, D. H. (2006) A simple γ-backbone modification preorganizes peptide nucleic acid into a helical structure, *J. Am. Chem. Soc. 128*, 10258−10267.

BI700854R